

# QCD effects in electroweak $WZjj$ production at current and future hadron colliders

B. Jäger<sup>1</sup>, A. Karlberg<sup>2</sup>, S. Reinhardt<sup>1</sup>

<sup>1</sup> *Institute for Theoretical Physics, University of Tübingen, Auf der Morgenstelle 14, 72076 Tübingen, Germany*

<sup>2</sup> *CERN, Theoretical Physics Department, CH-1211 Geneva 23, Switzerland*

## Abstract

We present new features for the implementation of  $WZjj$  production via vector-boson scattering in the framework of the POWHEG BOX program. In particular, previously unavailable semi-leptonic and fully hadronic decay modes of the intermediate vector bosons are provided, and operators of dimension six in an effective-field theory approach to account for physics beyond the Standard Model in the electroweak sector are included. For selected applications phenomenological results are provided to illustrate the capabilities of the new program. The impact of the considered dimension-six operators on experimentally accessible distributions is found to be small for current LHC energies, but enhanced in the kinematic reach of a potential future hadron collider with an energy of 100 TeV. The relevance of fully accounting for spin correlations and off-shell effects in the decay system is explored by a comparison with results obtained with the MadSpin tool that are based on an approximate treatment of the leptonic final state resulting from vector boson scattering processes. For selected semi-leptonic and hadronic decay modes we demonstrate the sensitivity of realistic signal selection procedures on QCD corrections and parton-shower effects.

# 1 Introduction

Vector boson scattering (VBS) processes are a particularly appealing class of reactions for exploring the electroweak (EW) sector of the Standard Model (SM) and possible extensions thereof. In the context of the SM, cross sections for the scattering of the longitudinal modes of an EW gauge boson are unitarised by Higgs-boson exchange contributions. The underlying cancellation mechanism is sensitive to both the Higgs- and the gauge-boson sector with deviations from the SM in particle content or properties immediately affecting the relevant cross sections. This makes VBS one of the most promising classes of processes for the discovery of physics beyond the SM in the EW sector.

In hadronic collisions the scattering of EW gauge bosons can be accessed in VBS processes which involve the scattering of hadronic constituents by EW gauge boson exchange. The experimental signature of such a reaction includes the gauge bosons' decay products and two distinctive jets resulting from the scattered partons. Because of the colour-singlet nature of the  $t$ -channel gauge-boson exchange these so-called tagging jets tend to be located in the far forward and backward regions of the detector with a large separation in rapidity. This feature of VBS reactions helps to identify the signal in the presence of QCD background processes with large production rates but rather different signatures.

At the CERN Large Hadron Collider (LHC), the ATLAS collaboration reported the observation of EW  $W^\pm Z jj$  production at a center-of-mass energy of  $\sqrt{s} = 13$  TeV in final states with three identified leptons of electron or muon type in 2018 [1]. The CMS collaboration observed the production of  $W^\pm Z$  pairs with leptonic decays in association with two jets at  $\sqrt{s} = 13$  TeV in 2020, and also provided constraints on anomalous quartic vector boson interactions [2]. In refs. [3, 4], semi-leptonic decay modes were considered.

In all of these experimental publications, however, the signal simulation was severely limited in accuracy: Refs. [1, 2, 4] resorted to a leading-order approximation of the signal process. In ref. [3] NLO-QCD corrections to the on-shell  $WZjj$  production process were taken into account, but a factorised ansatz was used to simulate the subsequent decay of the gauge-boson system. This approximation works reasonably well in the resonance region, but fails to provide an accurate description in other regions of phase space, as will be illustrated below.

In this article we specifically consider the VBS-induced  $W^\pm Z jj$  process taking next-to-leading-order (NLO) QCD corrections, off-shell effects, and spin correlations in the decay system fully into account. We provide implementations for the leptonic, semi-leptonic, and fully hadronic decay modes of the EW gauge bosons, and also explore how a generic extension of the SM affects experimentally accessible observables related to the tagging jets or the gauge bosons' decay products. Our work builds on an existing implementation of VBS-induced  $\bar{\nu}_e e^- \mu^- \mu^+ jj$  and  $\nu_e e^+ \mu^- \mu^+ jj$  production in the context of the SM. In ref. [5] the NLO-QCD corrections for these reactions as calculated in [6] have been implemented in the POWHEG BOX [7], a framework for the matching of a fixed-order perturbative calculation with parton shower (PS) programs using the POWHEG formalism [8, 9]. Here, we go beyond this existing implementation by adding semi-leptonic and hadronic decays of the gauge bosons, and considering an extension of the SM using the effective field theory (EFT) approach of ref. [10] that has already been used in the related  $ZZjj$

VBS process [11]. In addition, we investigate the relevance of off-shell effects and spin correlations in the decays by an explicit comparison to approximate treatments of these effects. We would like to point out the existence of a complementary calculation [12] for EW  $W^+Zjj$  calculation in the fully leptonic decay mode which focuses on perturbative corrections and provides results including the full NLO QCD and EW corrections. This calculation has, however, not been matched to a parton shower.

The article is structured as follows: In sec. 2 we describe the features of the updated implementation of EW  $WZjj$  production in hadronic collisions in the `POWHEG BOX`. Using this program, we present some representative numerical results of EW  $WZjj$  production at the LHC and a potential future circular hadron collider (FCC) operating at an energy of 100 TeV. We conclude in sec. 4.

## 2 Details of the POWHEG BOX implementation

In order to provide a Monte-Carlo program for the simulation of EW  $WZjj$  production in hadronic collisions at NLO+PS accuracy with the option for various leptonic, semi-leptonic, and hadronic final states in the context of the SM and a generic model supporting anomalous interactions in the gauge boson sector we provide appropriate extensions of the public `POWHEG BOX` implementation of Ref. [5].

We recall that this existing program resorts to tree-level and NLO-QCD matrix elements for the purely EW processes  $pp \rightarrow \nu_e e^+ \mu^- \mu^+ jj$  and  $pp \rightarrow \bar{\nu}_e e^- \mu^- \mu^+ jj$  adapted from the `VBFNLO` parton-level Monte-Carlo generator [13]. Even though in the following referred to as “EW  $WZjj$  production” for the sake of brevity, it is implicitly understood that all resonant and non-resonant diagrams giving rise to a  $\nu_e e^+ \mu^- \mu^+ jj$  or  $\bar{\nu}_e e^- \mu^- \mu^+ jj$  final state system are taken into account within the so-called VBS approximation. The VBS approximation only retains contributions from  $t$ -channel and  $u$ -channel diagrams, but not their interference, and disregards  $s$ -channel contributions. When selection cuts typical for an experimental VBS analysis are applied this approximation has been found [14] to reproduce the full result for the VBS cross section very well. For instance, for a representative setup at LO the authors of [14] report an agreement at the level of 0.6% between calculations based on full matrix elements and predictions of `VBFNLO` within the VBS approximation. We note, however, that the validity of this approximation deteriorates when more inclusive selection cuts are applied, see e.g. Ref. [15] for a comprehensive study of the VBS approximation. For this reason we only consider analysis setups with tight VBS cuts in sec. 3. The Cabibbo-Kobayashi-Maskawa matrix is assumed to be diagonal, and contributions from external top or bottom quarks are not taken into account. For the updated `POWHEG BOX` implementation of the EW  $WZjj$  production process presented here we resort to the same approximations.

As long as fully leptonic decays of the gauge bosons are considered, within the mentioned approximations the structure of the NLO-QCD corrections does not change if new interactions in the EW gauge-boson sector are taken into account. The original SM amplitudes for  $\nu_e e^+ \mu^- \mu^+ jj$  and  $\bar{\nu}_e e^- \mu^- \mu^+ jj$  production are structured in a modular way with leptonic tensors for those building blocks of the relevant Feynman diagrams that only contain colour-neutral particles, and hadronic currents accounting for the scattering

quarks and, in the real-emission contributions, gluons. The NLO-QCD corrections only affect the hadronic currents. Extensions of the SM in the EW sector thus merely require an appropriate replacement of the leptonic tensors.

We provide such an extension in the framework of the effective field theory (EFT) approach of Ref. [10] accounting for anomalous interactions in the EW gauge boson sector by an extension of the SM Lagrangian with operators of higher mass dimension,

$$\mathcal{L}_{\text{eff}} = \mathcal{L}_{\text{SM}} + \sum_{d>4} \sum_i \frac{c_i^{(d)}}{\Lambda^{d-4}} \mathcal{O}_i^{(d)}. \quad (1)$$

Here,  $d$  denotes the mass dimension of the operators  $\mathcal{O}_i^{(d)}$ , and the  $c_i^{(d)}$  are the expansion coefficients. The sum over  $d$  includes contributions of all higher-dimensional operators starting from  $d = 6$ . The summation index  $i$  runs over all non-vanishing operators of a given mass dimension. The parameter  $\Lambda$  denotes the energy scale up to which the EFT is supposed to be valid. We assume  $\Lambda$  to be much larger than the EW scale and thus restrict ourselves to the contribution of operators up to dimension six.

Following Ref. [10] we consider three independent operators that conserve charge ( $C$ ) and parity ( $P$ ),

$$\mathcal{O}_{WWW} = \text{Tr}[\hat{W}_{\mu\nu} \hat{W}^{\nu\rho} \hat{W}_\rho^\mu], \quad (2)$$

$$\mathcal{O}_W = (D_\mu \Phi)^\dagger \hat{W}^{\mu\nu} (D_\nu \Phi), \quad (3)$$

$$\mathcal{O}_B = (D_\mu \Phi)^\dagger \hat{B}^{\mu\nu} (D_\nu \Phi), \quad (4)$$

and two  $C$  and/or  $P$  violating operators,

$$\mathcal{O}_{\tilde{W}WW} = \text{Tr}[\tilde{W}_{\mu\nu} \hat{W}^{\nu\rho} \hat{W}_\rho^\mu], \quad (5)$$

$$\mathcal{O}_{\tilde{W}} = (D_\mu \Phi)^\dagger \tilde{W}^{\mu\nu} (D_\nu \Phi). \quad (6)$$

These operators are constructed from the Higgs doublet field  $\Phi$  and the electroweak field strength tensors  $W_{\mu\nu}^a$  ( $a = 1, 2, 3$ ) and  $B_{\mu\nu}$ ,

$$W_{\mu\nu}^a = \partial_\mu W_\nu^a - \partial_\nu W_\mu^a - g\epsilon_{abc} W_\mu^b W_\nu^c, \quad (7)$$

$$B_{\mu\nu} = \partial_\mu B_\nu - \partial_\nu B_\mu, \quad (8)$$

with the  $U(1)$  and  $SU(2)$  gauge fields  $B_\mu$  and  $W_\mu^a$  and their respective couplings  $g'$  and  $g$ . The  $\sigma^a$  denote the Pauli matrices. The covariant derivative  $D_\mu$  is given by

$$D_\mu = \partial_\mu + igW_\mu^a \frac{\sigma^a}{2} + \frac{1}{2}ig'B_\mu, \quad (9)$$

and the modified field strength tensors  $\hat{W}_{\mu\nu}$  and  $\hat{B}_{\mu\nu}$  are defined by

$$\hat{W}_{\mu\nu} = ig \frac{\sigma^a}{2} W_{\mu\nu}^a, \quad (10)$$

$$\hat{B}_{\mu\nu} = \frac{i}{2}g'B_{\mu\nu}, \quad (11)$$

$$[D_\mu, D_\nu] = \hat{W}_{\mu\nu} + \hat{B}_{\mu\nu}, \quad (12)$$

while the modified dual field strength tensor is given by

$$\tilde{W}_{\mu\nu} = \epsilon_{\alpha\beta\mu\nu} \hat{W}^{\alpha\beta}. \quad (13)$$

To simplify our notation we denote the coefficients of the operators of eqs. (2)–(6) that appear in the EFT expansion of eq. (1) up to dimension six as

$$C_i \equiv \frac{c_i^{(6)}}{\Lambda^2}. \quad (14)$$

In the following, instead of a numbered index  $i$  we use the label of the corresponding operator to identify each operator coefficient. For instance,  $C_{WWW}$  is the properly normalized coefficient of the  $\mathcal{O}_{WWW}$  operator.

In the actual calculation of scattering cross sections care has to be taken to ensure a consistent EFT expansion up to the desired order in  $1/\Lambda^2$ . Schematically, the operators of different mass dimension enter in the relevant matrix elements squared as

$$\begin{aligned} |\mathcal{M}_{SM} + \mathcal{M}_{dim-6} + \mathcal{M}_{dim-8} + \dots|^2 &= \underbrace{|\mathcal{M}_{SM}|^2}_{\Lambda^0} + \underbrace{2Re(\mathcal{M}_{SM}\mathcal{M}_{dim-6}^*)}_{\Lambda^{-2}} \\ &+ \underbrace{|\mathcal{M}_{dim-6}|^2 + 2Re(\mathcal{M}_{SM}\mathcal{M}_{dim-8}^*)}_{\Lambda^{-4}} + \dots \end{aligned} \quad (15)$$

Thus, if one truncates the EFT expansion at order  $1/\Lambda^2$ , in addition to the pure SM contribution one should only keep the interference term  $2Re(\mathcal{M}_{SM}\mathcal{M}_{dim-6}^*)$ , and disregard the quadratic term  $|\mathcal{M}_{dim-6}|^2$ , which is part of the  $\mathcal{O}(1/\Lambda^4)$  result. However, in the past in many applications this quadratic term was considered as part of the “dimension six” results. Below we therefore consider both options and refer to them as **SM+lin** and **SM+quad**.

In addition to the  $\nu_e e^+ \mu^- \mu^+ jj$  and  $\bar{\nu}_e e^- \mu^- \mu^+ jj$  final states provided in ref. [5], in this work we also implemented EW production of a  $\bar{\nu}_e e^- \nu_\mu \bar{\nu}_\mu$ , a  $q\bar{q}' \mu^- \mu^+$ , a  $\bar{\nu}_e e^- Q\bar{Q}$ , a  $\nu_e e^+ Q\bar{Q}$ , or a  $q\bar{q}' Q\bar{Q}$  system, respectively, in association with two tagging jets (here  $q$  and  $Q$  refer to massless quarks of different types). Representative diagrams for the partonic channel  $uc \rightarrow us \bar{d}u \mu^+ \mu^-$  are shown in fig. 1. For each channel, not only resonant diagrams related to the leptonic or hadronic decay of a  $W$  or  $Z$  boson are taken into account, but also non-resonant diagrams resulting in the same final state. For simplicity we will refer to the previously listed processes (including off-resonant contributions) as fully leptonic, leptonic-invisible, semi-leptonic, and fully hadronic decay modes. In the case of semi-leptonic and fully hadronic decay modes we do not take QCD corrections to the decays into account, and we neglect QCD corrections connecting the  $WZjj$  production with the decay part of the considered final state. The latter type of corrections are expected to be negligible. Corrections to the hadronic decays of the  $Z$  and  $W$  bosons are accounted for by the multi-purpose Monte-Carlo programs matched to our NLO-QCD calculation.

For each final state, at Born level singularities in the production cross section arise from diagrams with the  $t$ -channel exchange of a photon of very low virtuality  $Q^2$ . Such contributions are entirely negligible after selection cuts on the tagging jets are applied and can thus be removed already at generation level by a cut,

$$Q_{\min}^2 = 4 \text{ GeV}^2. \quad (16)$$

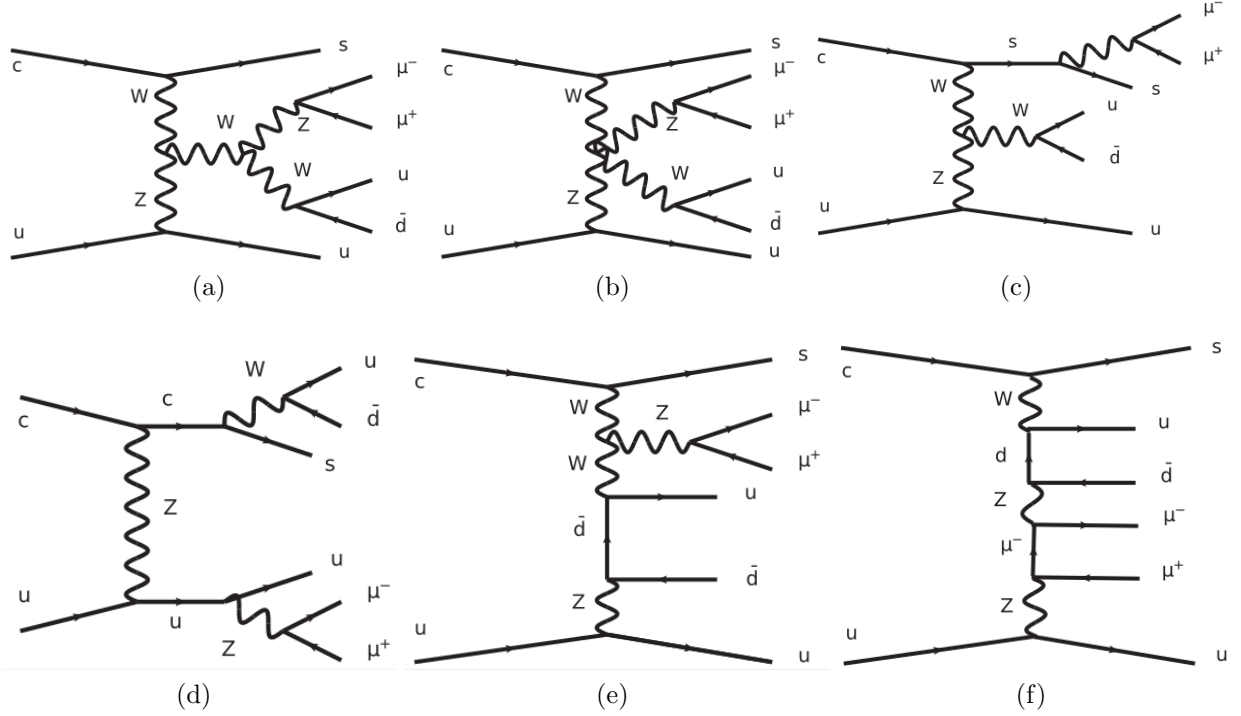


Figure 1: Representative Feynman diagrams for the VBS-process  $u c \rightarrow u s \bar{d} u \mu^+ \mu^-$ : (a),(b) genuine vector-boson scattering diagrams, (c),(d) diagrams including gauge-boson emission from a quark line, (e) singly-resonant, and (f) non-resonant diagrams.

To further improve the numerical efficiency of the Monte-Carlo integration additionally a Born-suppression factor of the form

$$F(\Phi) = \left( \frac{p_{T,1}^2}{p_{T,1}^2 + \Lambda_\Phi^2} \right)^2 \left( \frac{p_{T,2}^2}{p_{T,2}^2 + \Lambda_\Phi^2} \right)^2. \quad (17)$$

can be employed. Here, the  $p_{T,i}$  denote the transverse momenta of the final-state partons of the underlying Born configuration  $\Phi$ , and  $\Lambda_\Phi$  is a technical parameter, by default set to 10 GeV.

We remind the reader that contributions with a pair of same-type charged fermions ( $f$ ) in the final state cannot only stem from decays of the  $WZ$  system, but also from diagrams where a photon decays into a fermion pair. An additional type of singularity at Born level arises from diagrams where such a photon exhibits very low virtuality. For analyses that require a fermion pair with an invariant mass close to the mass of the  $Z$  boson, such singularities can easily be removed already at generation level by an invariant mass cut on the respective lepton pair. The requirement

$$m_{f\bar{f}} > 0.5 \text{ GeV} \quad (18)$$

suffices to remove any potentially problematic contributions from photons of very low virtuality at generation level.

### 3 Phenomenological results

In the following we will provide some phenomenological results generated by our implementation in version 2 of the `POWHEG BOX`. For all of these results we use the following general settings: We set the Fermi constant to  $G_\mu = 1.1663787 \cdot 10^{-5} \text{ GeV}^{-2}$ . For the masses and widths of the EW bosons we use:  $m_H = 125.25 \text{ GeV}$ ,  $m_W = 80.377 \text{ GeV}$ ,  $m_Z = 91.1876 \text{ GeV}$ ,  $\Gamma_H = 0.0032 \text{ GeV}$ ,  $\Gamma_W = 2.085 \text{ GeV}$ , and  $\Gamma_Z = 2.4952 \text{ GeV}$ . The EW coupling,  $\alpha_{em}$ , is calculated therefrom via tree-level EW relations.

In addition to the `POWHEG BOX` we also use the tool-chain `MadGraph5_aMC@NLO` [16, 17] including the program `MadSpin` [18] for comparison to the `POWHEG BOX` results. To simulate the parton shower we use `PYTHIA8`, version 8.245, with the `Monash2013` tune [19]. Hadronisation, MPI, and QED emissions are turned off. For reconstructing jets we resort to `FastJet` [20], version 3.3.4. For all results presented in this section jets are clustered via the anti- $k_T$  algorithm [21] with a radius-parameter of  $R = 0.4$ , and the `NNPDF31_nlo_as_0118` (ID 303400) set [22] of parton distribution functions (PDFs) is used as provided by version 6.3.0 of the `LHAPDF` library [23].

#### 3.1 EFT results

In this subsection we explore the impact of SM extensions in the EFT framework introduced in sec. 2. We individually set the coefficient of each EFT operator defined in eqs. (2)-(6) to the largest value compatible with the experimental limits of ref. [24] while setting the coefficients of all other EFT operators to zero. As it turned out that the impact of the  $\mathcal{O}_{WWW}$  operator is most pronounced, below we only display results obtained for non-vanishing values of the  $C_{WWW}$  coefficient. For instance, results obtained with non-vanishing values of the  $C_W$  operator coefficient are basically identical to the SM results and will thus not be further discussed here.

For the unitarisation of our EFT predictions we proceeded along the lines of ref. [25] where unitarity violations are avoided by using appropriate cuts on the invariant mass of the vector bosons produced in a VBS reaction. We calculated the limits beyond which unitarity violations are to be expected for the setups considered in this work using the tool `calc-formfactor` [26, 27] that is available within the `VBFNLO` package [28, 29]. We found that unitarity violations would occur only beyond scales relevant for the results shown below.

Throughout this subsection we use a renormalisation scale,  $\mu_R = \xi_R \mu_0$ , and factorisation scale,  $\mu_F = \xi_F \mu_0$ , that is expected to optimally account for the region of high transverse momenta where the effects of the dimension-six operators are expected to have the largest impact (c.f. ref. [11]). The scale  $\mu_0$  is given by

$$\mu_0 = \frac{1}{2} \left( E_{T,W} + E_{T,Z} + \sum_f^{n_{\text{part}}} p_{T,f} \right), \quad (19)$$

where the sum includes the transverse momenta  $p_{T,f}$  of all  $n_{\text{part}}$  final-state partons of a considered Born-type or real-emission configuration. In addition we define

$$E_{T,W} = \sqrt{m_W^2 + p_{T,W}^2}, \quad E_{T,Z} = \sqrt{m_Z^2 + p_{T,Z}^2}, \quad (20)$$

where  $p_{T,Z}$  and  $p_{T,W}$  are the transverse momenta of the muon pair and the positron-neutrino pair of the fixed-order configuration, respectively. The factors  $\xi_R$  and  $\xi_F$  are varied between 0.5 and 2 with 7-point variation in our NLO+PS simulations and set to one for the fixed-order calculations.

For our representative numerical studies we use settings inspired by the ATLAS analysis described in ref. [30]. In particular, we construct jets using the anti- $k_T$  algorithm with  $R = 0.4$ . In the following we will denote the jets with index  $j_1$  for the hardest jet and  $j_2, j_3, \dots$  for further jets ordered by their transverse momentum. The two hardest jets are identified as tagging jets and are required to have a transverse momentum, rapidity and invariant mass of

$$p_{T,j}^{\text{tag}} > 30 \text{ GeV}, \quad |y_j^{\text{tag}}| < 4.5, \quad m_{jj}^{\text{tag}} > 500 \text{ GeV}. \quad (21)$$

Moreover, we only keep events where the tagging jets lie in opposite hemispheres,

$$\eta_{j_1}^{\text{tag}} \cdot \eta_{j_2}^{\text{tag}} < 0, \quad (22)$$

and have a large rapidity separation of

$$\Delta y_{jj}^{\text{tag}} = |y_{j_1}^{\text{tag}} - y_{j_2}^{\text{tag}}| \geq 2.5. \quad (23)$$

To identify additional non-tagging jets we require them to be located in a rapidity range of

$$|y_j| < 4.5. \quad (24)$$

No other cuts are applied on non-tagging jets unless specifically stated otherwise.

In our fixed-order results the final state contains two muons, one positron and one neutrino. Within the PYTHIA setup we consider, i.e. in the absence of QED radiation in the parton shower and without hadron decays, the events we simulate at NLO+PS level do not exhibit any additional leptons or neutrinos. For the charged leptons  $\ell$  we demand

$$p_{T,\ell} > 15 \text{ GeV}, \quad |y_\ell| < 2.5. \quad (25)$$

We do not apply any cuts on the neutrino. Furthermore, we require a clear separation of the tagging jets and the charged leptons, i.e. we require a separation in the rapidity-azimuthal angle plane of

$$R_{j\ell} > 0.3. \quad (26)$$

For the muons which are stemming from the  $Z$  decay we additionally demand

$$R_{\mu\mu} > 0.3, \quad (27)$$

as well as that their reconstructed invariant mass,  $m_{\text{inv}}^Z$ , lies in a window around the physical  $Z$ -boson mass of

$$66 \text{ GeV} < m_{\text{inv}}^Z < 116 \text{ GeV}. \quad (28)$$

Finally, we also require all charged leptons to lie in the rapidity gap between the two tagging jets

$$\min(y_{j_1}^{\text{tag}}, y_{j_2}^{\text{tag}}) < y_\ell < \max(y_{j_1}^{\text{tag}}, y_{j_2}^{\text{tag}}). \quad (29)$$

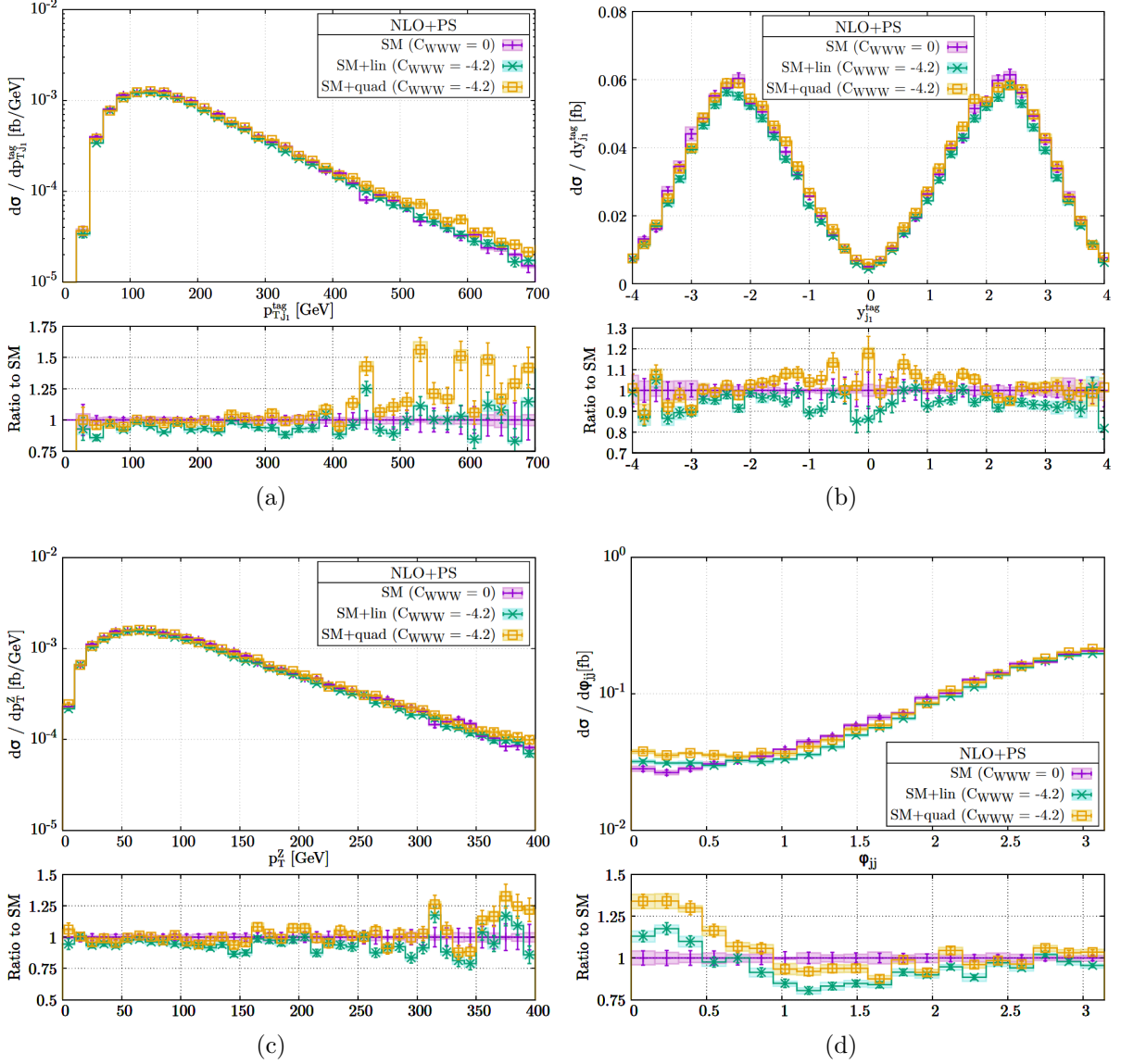


Figure 2: NLO+PS predictions for  $pp \rightarrow \nu_e e^+ \mu^- \mu^+ jj$  at the LHC with  $\sqrt{s} = 13$  TeV within the cuts of eqs. (21)–(29) for the SM+lin (green) and the SM+quad case (orange) with  $C_{WWW} = -4.2 \text{ TeV}^{-2}$ , and within the SM (purple). The upper panels show the transverse momentum of the hardest tagging jet (a), the rapidity of the hardest tagging jet (b), the reconstructed transverse momentum of the  $Z$  boson (c), and the azimuthal angle separation of the tagging jets (d). The respective lower panels show the ratios of the SM+lin and SM+quad predictions to the pure SM results.

Let us now discuss results for the LHC with a center-of-mass energy of  $\sqrt{s} = 13$  TeV. In fig. 2 and fig. 3 we compare SM results at NLO+PS accuracy for selected distributions of the tagging jets and the leptons with those obtained in the EFT framework of sec. 2. In particular, we set the operator coefficient  $C_{WWW}$  to the maximal negative value compatible with current experimental limits, i.e.  $C_{WWW} = -4.2 \text{ TeV}^{-2}$ , and consider separately

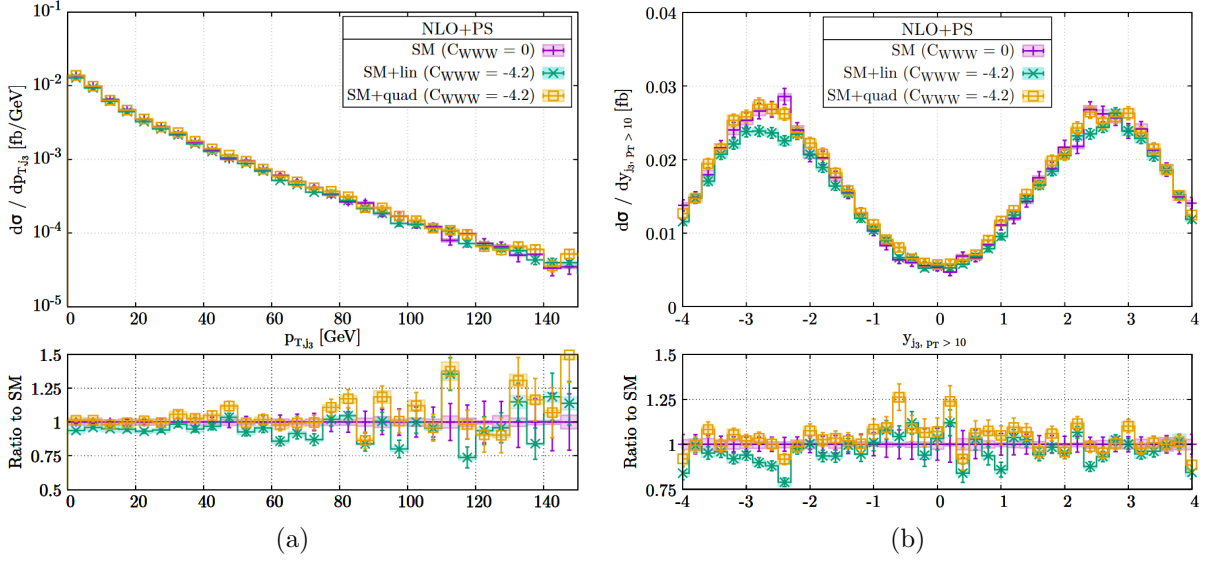


Figure 3: NLO+PS predictions for  $pp \rightarrow \nu_e e^+ \mu^- \mu^+ jj$  at the LHC with  $\sqrt{s} = 13$  TeV within the cuts of eqs. (21)–(29) for the **SM+lin** (green) and the **SM+quad** case (orange) with  $C_{WW} = -4.2 \text{ TeV}^{-2}$ , and within the SM (purple). The upper panels show the transverse momentum of the 3rd jet (a) and the rapidity of the 3rd jet for a  $p_T$  cut of  $p_{T,j_3} > 10 \text{ GeV}$  (b). The respective lower panels show the ratios of the **SM+lin** and **SM+quad** predictions to the pure SM results.

the case where only the linear term of the EFT expansion sketched in eq. (15) is taken into account (dubbed **SM+lin**), and the case where additionally the quadratic term is retained (referred to as **SM+quad**).

For the **SM+lin** implementation we find only small differences to the SM results for all considered distributions. These effects are best visible for the azimuthal angle separation of the two tagging jets,  $\Phi_{jj}$ . In particular for  $\Phi_{jj} \lesssim \pi/2$  the shape is slightly different from the SM case. Larger differences to the SM case are found for the **SM+quad** implementation. However, we would like to remind the reader that the limits chosen for  $C_{WW}$  have been derived for the **SM+lin** implementation and that the **SM+quad** version is shown only for the purpose of comparison. The **SM+lin** and **SM+quad** predictions can barely be distinguished from the respective SM results for the transverse momentum and the rapidity distributions of the hardest tagging jet and the transverse momentum of the  $Z$  boson. The latter is reconstructed from the momenta of the muon pair closest in invariant mass to  $m_Z$ .

In fig. 4 and fig. 5 we display the same observables as in fig. 2 and fig. 3 for a potential future circular collider (FCC) with proton-proton collisions at a center-of-mass energy of  $\sqrt{s} = 100$  TeV. For the FCC discussion we use the following setup inspired by ref. [31]. We use the same renormalisation and factorisation scale as in eq. (19), but apply stronger cuts on the tagging jets. More precisely, we require

$$p_{T,j}^{\text{tag}} > 50 \text{ GeV}, \quad |y_j^{\text{tag}}| < 6, \quad m_{jj}^{\text{tag}} > 2500 \text{ GeV}. \quad (30)$$

Additionally, the tagging jets have to fulfill

$$\eta_{j_1}^{\text{tag}} \cdot \eta_{j_2}^{\text{tag}} < 0, \quad \Delta y_{jj}^{\text{tag}} = |y_{j_1}^{\text{tag}} - y_{j_2}^{\text{tag}}| \geq 5. \quad (31)$$

For the charged leptons we require

$$p_{T,\ell} > 20 \text{ GeV}, \quad |y_\ell| < 5, \quad (32)$$

as well as a separation of the tagging jets and the charged leptons in the rapidity-azimuthal angle plane of

$$R_{j\ell} > 0.4. \quad (33)$$

We keep the requirements of eqs. (27)–(29).

Differences between the SM and the **SM+quad** implementation are clearly enhanced at this energy for all distributions. However, the azimuthal angle separation of the tagging jets exhibits sensitivity to the effects of the **SM+lin** implementation.

### 3.2 Leptonic decays

The objective of this subsection is to explore the relevance of simulating the full leptonic final state of VBS-induced  $\bar{\nu}_e e^- \mu^- \mu^+ jj$  production as opposed to approximations where a  $W^+ Z$  boson pair is produced on-shell and combined with a simulation for the decays of these bosons into the desired leptonic final state. Such an approximation is used, for instance, in the search for anomalous EW production of vector boson pairs in association with two jets by the CMS collaboration [4] and in the search for EW diboson production in association with a high-mass dijet system in semi-leptonic final states by the ATLAS collaboration [3]. Since QCD corrections do not directly affect the leptonic decays, we conduct this discussion at LO. To that end we compare our **POWHEG BOX** implementation for  $\bar{\nu}_e e^- \mu^- \mu^+ jj$  production via VBS with two alternative ones: The first is using **MadGraph5\_aMC@NLO** where a  $W^+ Z jj$  final state is produced on-shell. The decays of the two bosons are afterwards simulated via **MadSpin** (this simulation is denoted by **MG5+MadSpin** below). The other implementation is using the LO version of **MadGraph5\_aMC@NLO** and includes off-shell contributions and spin-correlations in the lepton system (this implementation will be denoted by **MG5-full** in the following). This comparison serves as a consistency check for the correct usage of the two tools. It also shows the equivalence of the **POWHEG BOX** and the **MG5-full** implementation after the application of VBS cuts despite more approximations being used in the matrix elements entering the **POWHEG BOX** than the **MG5-full** implementation.

For the comparison presented in this subsection we use a fixed factorisation and renormalisation scale of

$$\mu_F = \mu_R = m_W / \sqrt{1 + (\Gamma_W/m_W)^2}. \quad (34)$$

As before, we consider proton collisions at the LHC with  $\sqrt{s} = 13 \text{ TeV}$ . For the selection of signal events we proceed along similar lines as in the previous subsection. We impose the cuts of eqs. (21)–(29) defined above.

In fig. 6 we show several distributions related to the decay system of the VBS-induced  $\nu_e e^+ \mu^- \mu^+ jj$  production process. The invariant masses of the  $W$  and  $Z$  systems,  $m_{\text{inv}}^W$  and

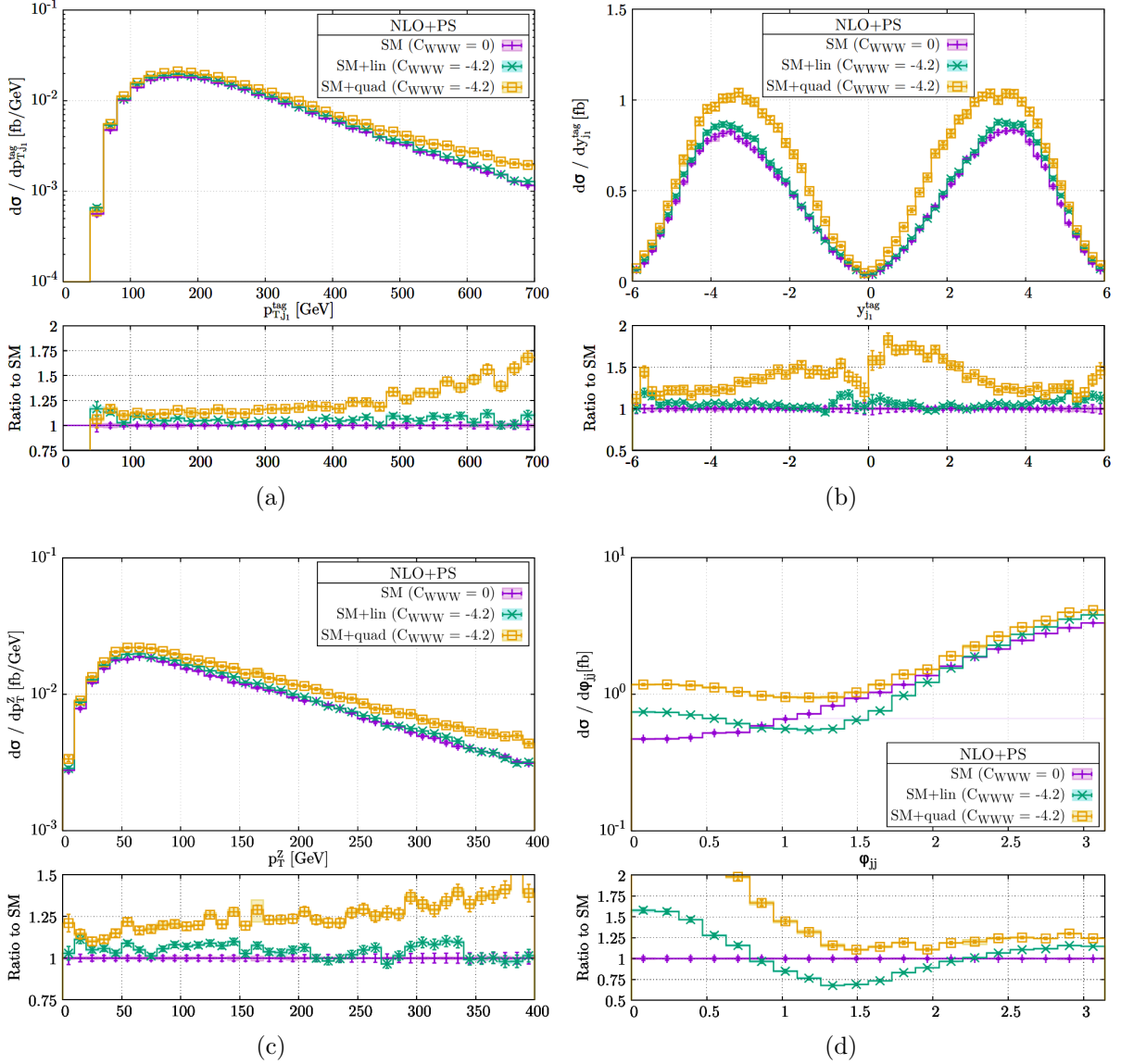


Figure 4: Same as in fig. 2, but for the FCC with an energy of  $\sqrt{s} = 100$  TeV and with the cuts of eqs. (27)–(33).

$m_{\text{inv}}^Z$ , are reconstructed from the momenta of the  $\nu_e e^+$  and  $\mu^- \mu^+$  pairs, respectively. The transverse mass of the  $WZ$  system is defined by

$$m_T(WZ) = \sqrt{(\tilde{E}_{T,W} + \tilde{E}_{T,Z})^2 - (p_{T,W} + p_{T,Z})^2}, \quad (35)$$

where  $p_{T,W}$  and  $p_{T,Z}$  are the transverse momenta of the reconstructed  $W$  and  $Z$  systems, and the transverse energies  $\tilde{E}_{T,i}$  ( $i = W, Z$ ) are given by

$$\tilde{E}_{T,i} = \sqrt{(m_{\text{inv}}^i)^2 + p_{T,i}^2}. \quad (36)$$

We find that, for each considered distribution, the results of the **MG5-full** and the **POWHEG BOX** implementations are in very good agreement within their respective statistical

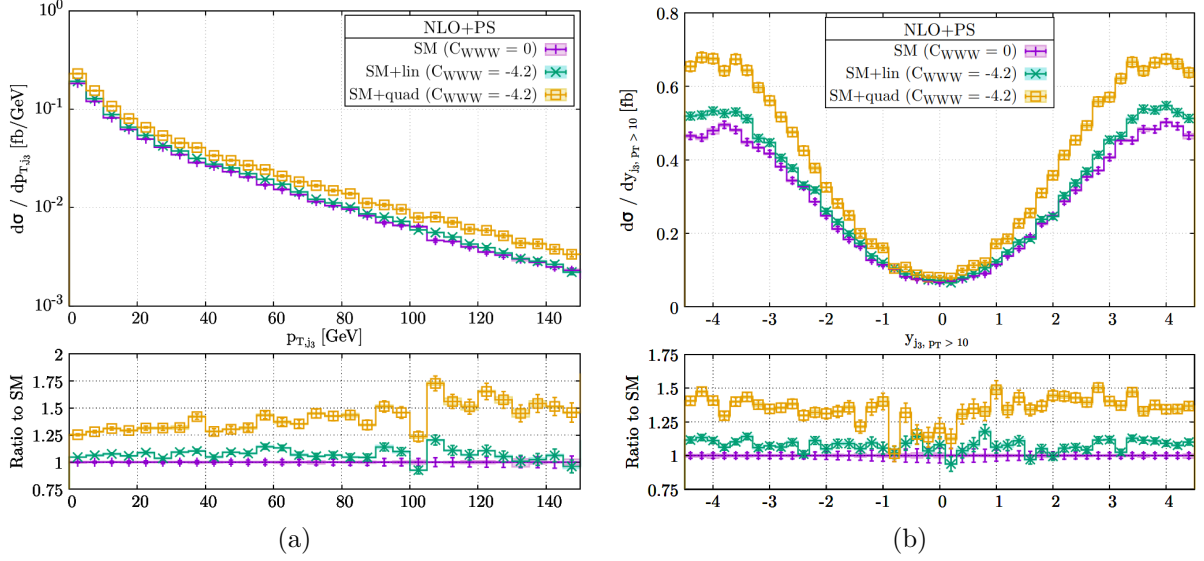


Figure 5: Same as in fig. 3, but for the FCC with an energy of  $\sqrt{s} = 100$  TeV and with the cuts of eqs. (27)–(33).

uncertainties. In contrast, the results of **MG5+MadSpin** deviate from the implementations that retain full control on off-shell contributions and spin correlations in the leptonic decay system. While near the  $W$  and  $Z$  resonances **MG5+MadSpin** yields satisfactory results, further away from the peaks of the invariant mass distributions, and in particular in the tails of the transverse mass distribution, the on-shell approximation does no longer accurately reproduce the full results. Deviations can reach almost an order of magnitude for  $m_T(WZ) \lesssim 150$  GeV and  $m_T(WZ) \gtrsim 350$  GeV. This should be kept in mind for the simulation of VBS processes when off-shell regions are of interest.

### 3.3 Semi-leptonic and hadronic decays

While in ref. [5] an implementation for VBS-induced  $WZ$  production with fully leptonic decays was developed and made available in the **POWHEG BOX** program package, semi-leptonic and fully hadronic final states were not considered before in that framework. We have closed this gap and are now able to simulate all possible decay modes of the  $WZ$  system in the VBS mode.

As an example for a semi-leptonic decay mode in this subsection we provide phenomenological results for the VBS process where a  $W^+$  boson decays hadronically into an  $u\bar{d}$  pair, and the  $Z$  boson into a muon pair. All off-shell diagrams giving rise to the same final state are taken into account, see fig. 1.

The decay quarks of the  $W$  boson give rise to jets. For the selection of the VBS signal in the presence of background processes it is important to distinguish these decay jets from the tagging jets of the production process. The representative numerical analysis below is designed to take that into account.

Throughout this subsection we use the dynamical scale of eq. (19). For the selection of events in the semi-leptonic mode at the LHC with an energy of  $\sqrt{s} = 13$  TeV we impose

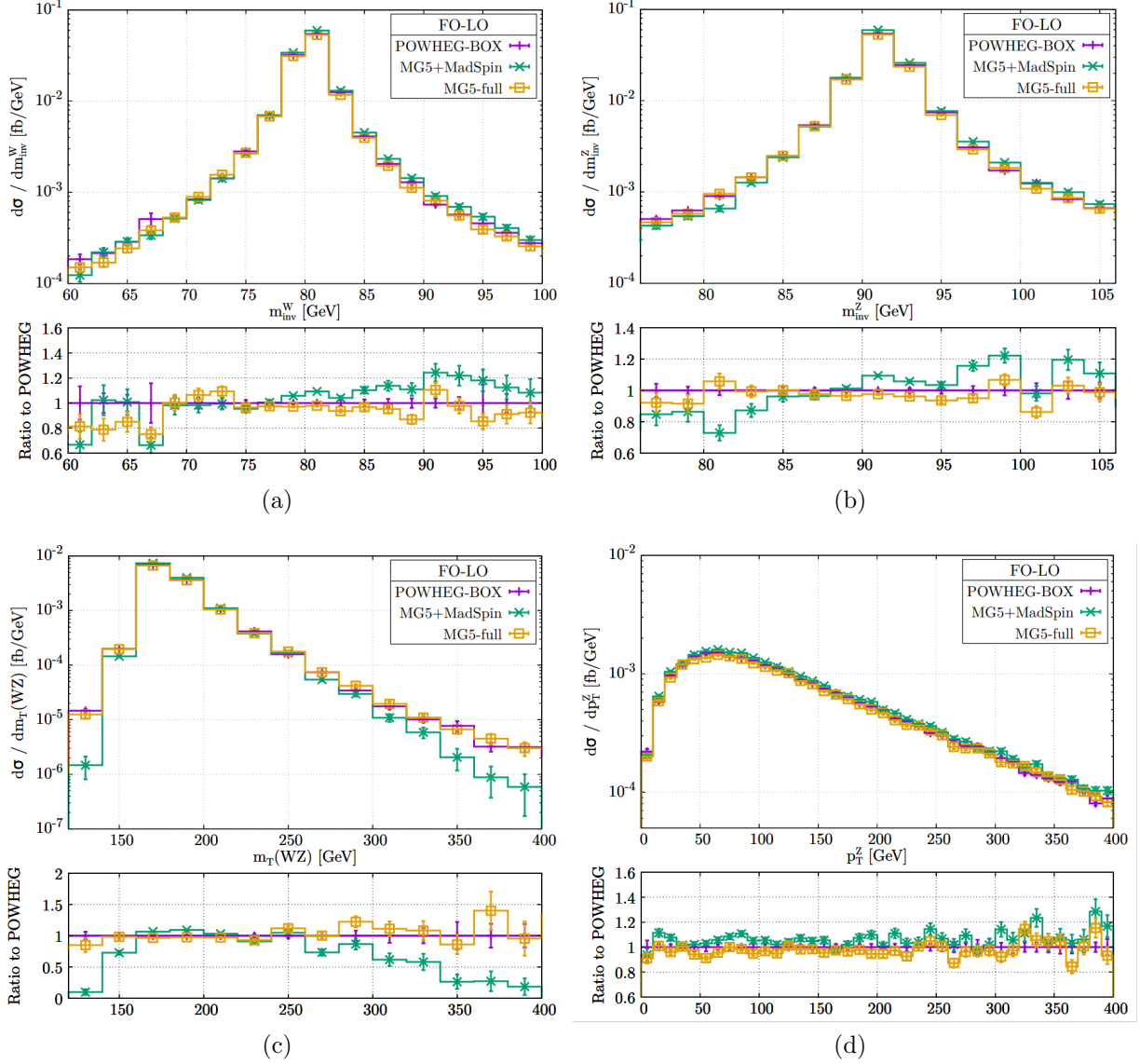


Figure 6: LO predictions for  $pp \rightarrow \nu_e e^+ \mu^- \mu^+ jj$  at the LHC with  $\sqrt{s} = 13$  TeV within the cuts of eqs. (21)-(29) as obtained with the POWHEG-BOX (purple), MG5+MadSpin (green), and with MG5-full (orange). The upper panels show the reconstructed invariant mass of the  $W$  boson (a), the reconstructed invariant mass of the  $Z$  boson (b), the transverse mass of the  $WZ$  system (c), and the reconstructed transverse momentum of the  $Z$  boson (d). The respective lower panels show the ratios of the MG5+MadSpin and MG5-full predictions to the POWHEG-BOX results.

the following cuts: Charged leptons are required to fulfill the basic requirements

$$p_{T,\ell} > 20 \text{ GeV}, \quad |y_\ell| < 2.47. \quad (37)$$

For the hardest lepton we additionally request

$$p_{T,\ell}^{\text{hardest}} > 28 \text{ GeV}. \quad (38)$$

Furthermore, the invariant mass reconstructed from the muon pair has to fulfill

$$83 \text{ GeV} < m_{\text{inv}}^Z < 99 \text{ GeV}. \quad (39)$$

Jets and the leptons have to be separated by

$$R_{j\ell} > 0.4. \quad (40)$$

We require all jets to have

$$p_{T,j} > 20 \text{ GeV}, \quad |y_j| < 4.5. \quad (41)$$

The jets in an event are then further classified. The decay jets are identified as those two jets with the invariant mass being closest to the mass of the  $W$  boson. These two jets are required to lie within a window around the  $W$  mass of

$$64 \text{ GeV} < m_{\text{inv}}^W < 106 \text{ GeV}, \quad (42)$$

and to fulfill the transverse-momentum requirements

$$p_{T,j_1}^{\text{dec}} > 40 \text{ GeV}, \quad p_{T,j_2}^{\text{dec}} > 30 \text{ GeV}, \quad (43)$$

where  $j_1$  and  $j_2$  denote the hardest and second hardest decay jets.

After the selection of the decay jets, the two hardest remaining jets are identified as the tagging jets. For the tagging jets we require

$$p_{T,j}^{\text{tag}} > 30 \text{ GeV}, \quad m_{jj}^{\text{tag}} > 400 \text{ GeV}, \quad R_{jj} > 0.4, \quad \eta_{j_1}^{\text{tag}} \cdot \eta_{j_2}^{\text{tag}} < 0. \quad (44)$$

Fig. 7 and fig. 8 display some representative distributions related to the tagging jets and the decay jets at LO, NLO, and NLO+PS accuracy. As expected, tagging jets and decay jets exhibit entirely different properties. Both, transverse momentum and rapidity distributions look very different for the two types of jets. From the rapidity distributions one can understand that the decay jets are preferentially located at central rapidities, while the tagging jets peak in the forward and backward regions, analogous to the leptonic decay mode. We note that generally the curves for the NLO+PS results lie below the fixed-order predictions, indicating smaller event rates. As can be deduced from the invariant mass distribution in fig. 8 (b) the shift of momenta beyond LO results in a considerable change of shape in  $m_{\text{inv}}^W$ . However this quantity is used as a selection criterion (c.f. eq. (42)). With  $m_{\text{inv}}^W$  shifted to values further away from  $m_W$ , at NLO+PS level fewer events pass the selection criterion of eq. (42) resulting in a smaller value of the associated cross section.

Let us now consider a representative fully hadronic decay mode with the  $W^+$  boson decaying into a  $u\bar{d}$  pair and the  $Z$  boson into a pair of  $s$  quarks. The large number of jets emerging from this mode requires a dedicated analysis allowing for a proper classification of tagging and decay jets.

We require all jets to have

$$p_{T,j} > 10 \text{ GeV}, \quad |y_j| < 4.5. \quad (45)$$

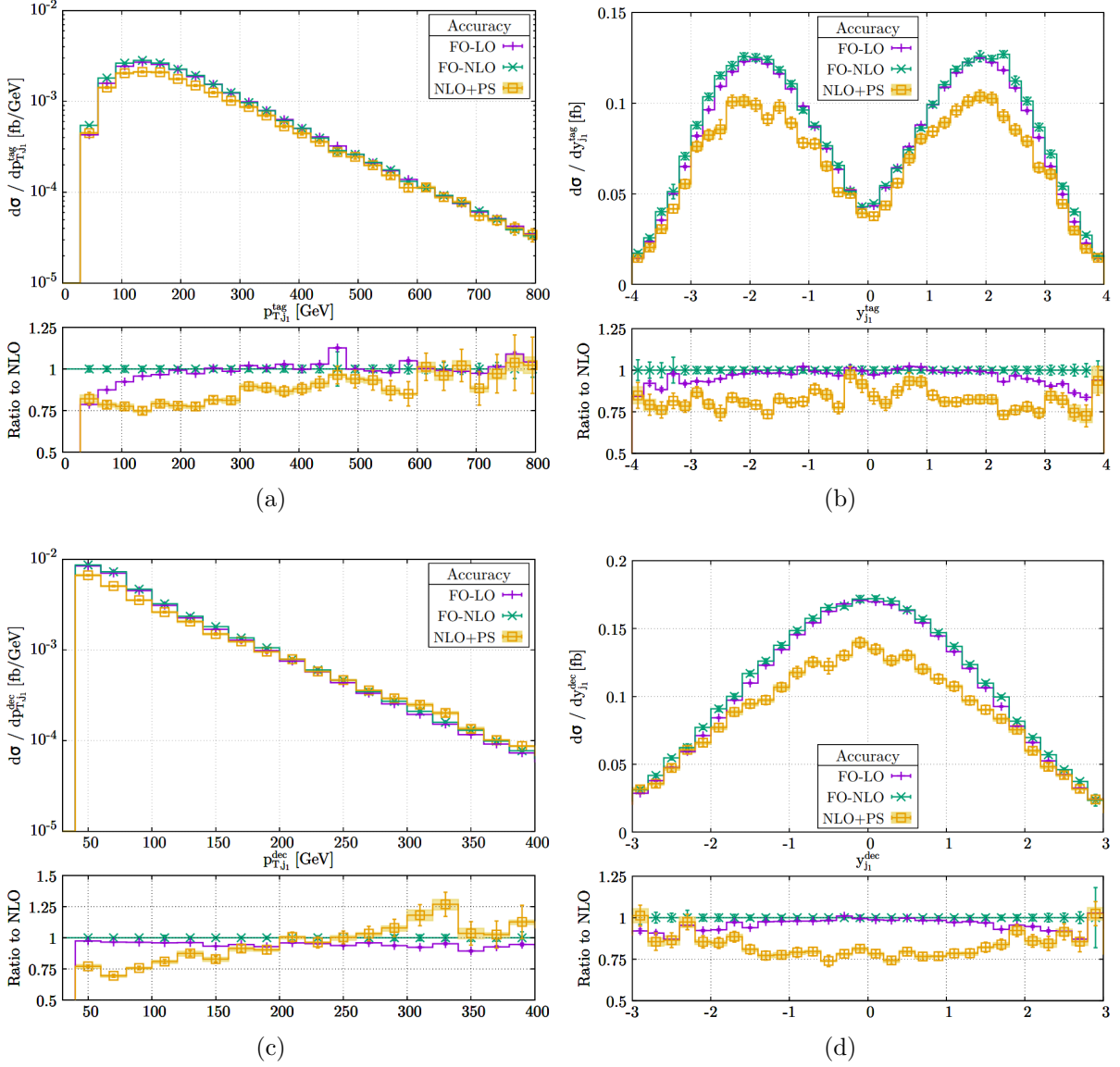


Figure 7: Predictions for VBS-induced  $W^+Z$  production in the semi-leptonic decay mode at the LHC with  $\sqrt{s} = 13$  TeV within the cuts of eqs. (37)–(44) at LO (purple), NLO (green) and NLO+PS (orange). The upper panels show the transverse momentum of the hardest tagging jet (a), the rapidity of the hardest tagging jet (b), the transverse momentum of the hardest decay jet (c), the rapidity of the hardest decay jet (d). The respective lower panels show the ratios of the LO and NLO+PS predictions to the NLO results.

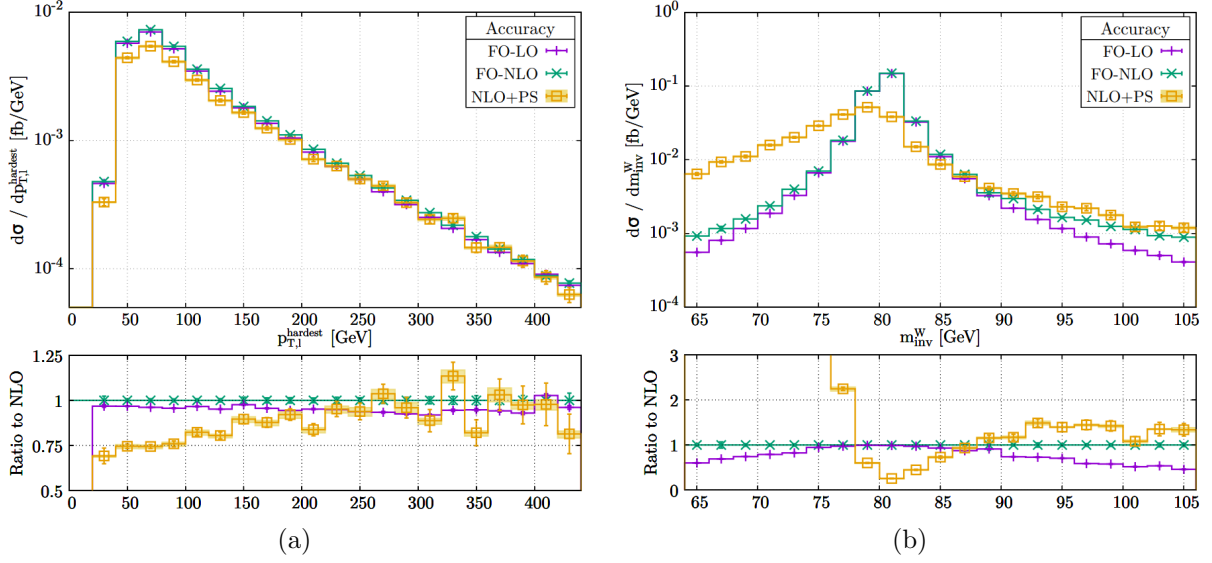


Figure 8: Predictions for VBS-induced  $W^+Z$  production in the semi-leptonic decay mode at the LHC with  $\sqrt{s} = 13$  TeV within the cuts of eqs. (37)–(44) at LO (purple), NLO (green) and NLO+PS (orange). The upper panels show the transverse momentum of the hardest lepton (a) and the reconstructed invariant mass of the  $W$ -boson system (b). The respective lower panels show the ratios of the LO and NLO+PS predictions to the NLO results.

To identify the jets associated with the decay of the  $W$  and  $Z$  boson we proceed in the following way: In the first step, from all pairs of jets we choose the one with its invariant mass closest to  $m_W$ . These two jets are then considered to correspond to the decay of the  $W$  boson. In a second step, we proceed analogously for the  $Z$  boson (replacing  $m_W$  with  $m_Z$ ). In a third step, we check if a jet is contained in both the jet-pair associated with the  $W$  boson and the one associated with the  $Z$  boson. If this is the case we assign it to the boson with mass closer to the corresponding jet-pair. In a fourth step, we repeat the first or second step for the boson that was not chosen in the third step with the remaining jets not assigned to the other boson. The jets having thus been associated with the  $W$  and  $Z$  decays have to fulfill the transverse-momentum requirements of

$$\begin{aligned} p_{T,j_1}^{W-\text{dec}} &> 20 \text{ GeV}, & p_{T,j_2}^{W-\text{dec}} &> 10 \text{ GeV}, \\ p_{T,j_1}^{Z-\text{dec}} &> 20 \text{ GeV}, & p_{T,j_2}^{Z-\text{dec}} &> 10 \text{ GeV}. \end{aligned} \quad (46)$$

and exhibit invariant masses close to the respective gauge-boson mass,

$$\begin{aligned} 64 \text{ GeV} &< m_{jj}^{W-\text{dec}} < 88 \text{ GeV}, \\ 84 \text{ GeV} &< m_{jj}^{Z-\text{dec}} < 106 \text{ GeV}. \end{aligned} \quad (47)$$

If an event does not pass these cuts, it is discarded.

After the selection of the decay jets, the two hardest remaining jets are identified as the tagging jets. As in the semi-leptonic case, for the tagging jets we additionally require

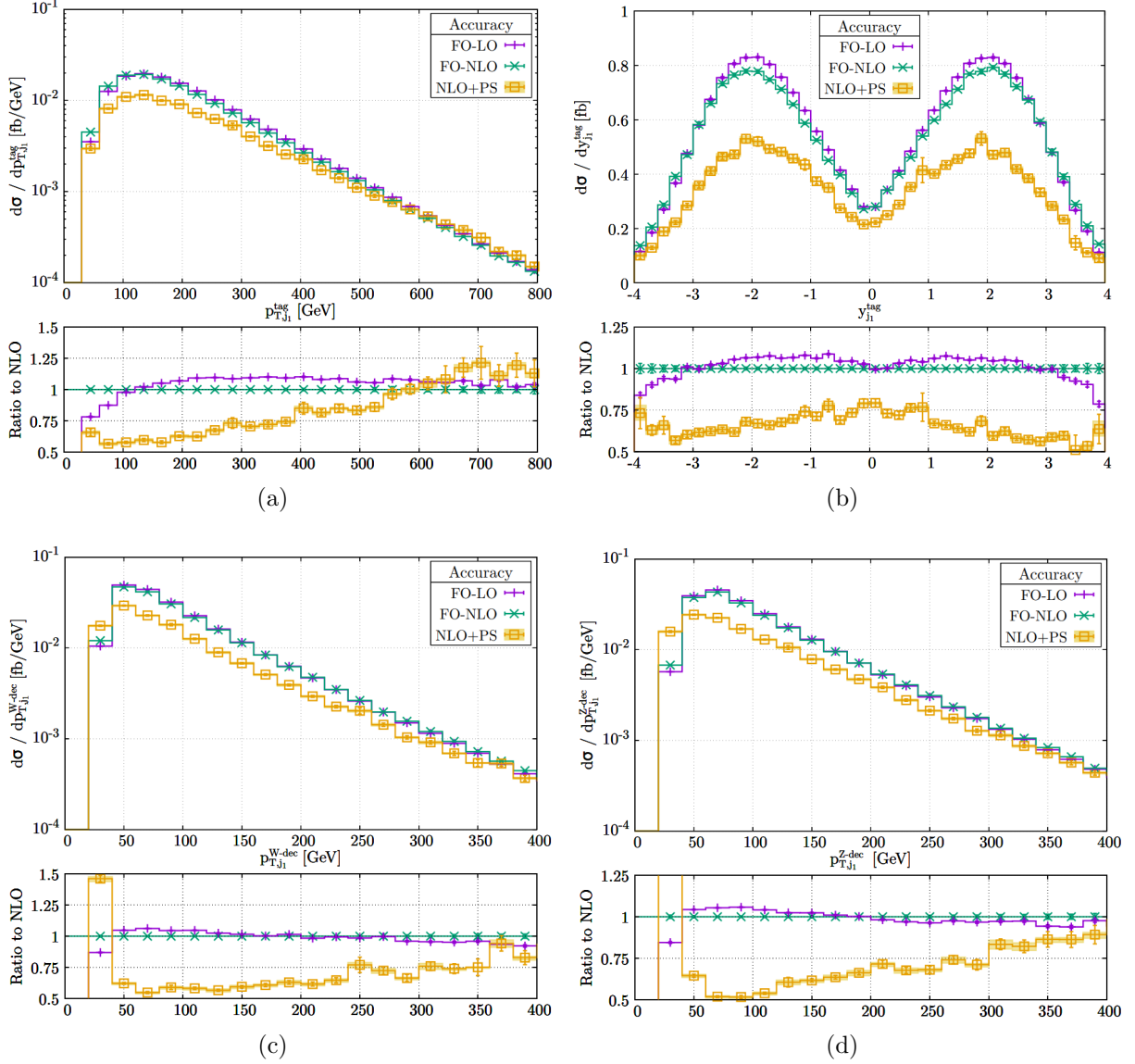


Figure 9: Predictions for VBS-induced  $W^+Z$  production in the fully hadronic decay mode at the LHC with  $\sqrt{s} = 13$  TeV within the cuts of eqs. (45)–(48) at LO (purple), NLO (green) and NLO+PS (orange). The upper panels show the transverse momentum of the hardest tagging jet (a), the rapidity of the hardest tagging jet (b), the transverse momentum of the hardest decay jet from the  $W$  decay (c), the transverse momentum of the hardest decay jet from the  $Z$  decay (d). The respective lower panels show the ratios of the LO and NLO+PS predictions to the NLO results.

$$p_{T,j}^{\text{tag}} > 30 \text{ GeV}, \quad m_{jj}^{\text{tag}} > 400 \text{ GeV}, \quad R_{jj} > 0.4, \quad \eta_{j_1}^{\text{tag}} \cdot \eta_{j_2}^{\text{tag}} < 0. \quad (48)$$

In fig. 9 and fig. 10 we show several distributions for the fully hadronic decay mode.

We observe results that are qualitatively similar to the semi-leptonic case discussed above. However, the “smearing effect” in the NLO+PS results is even larger than in the

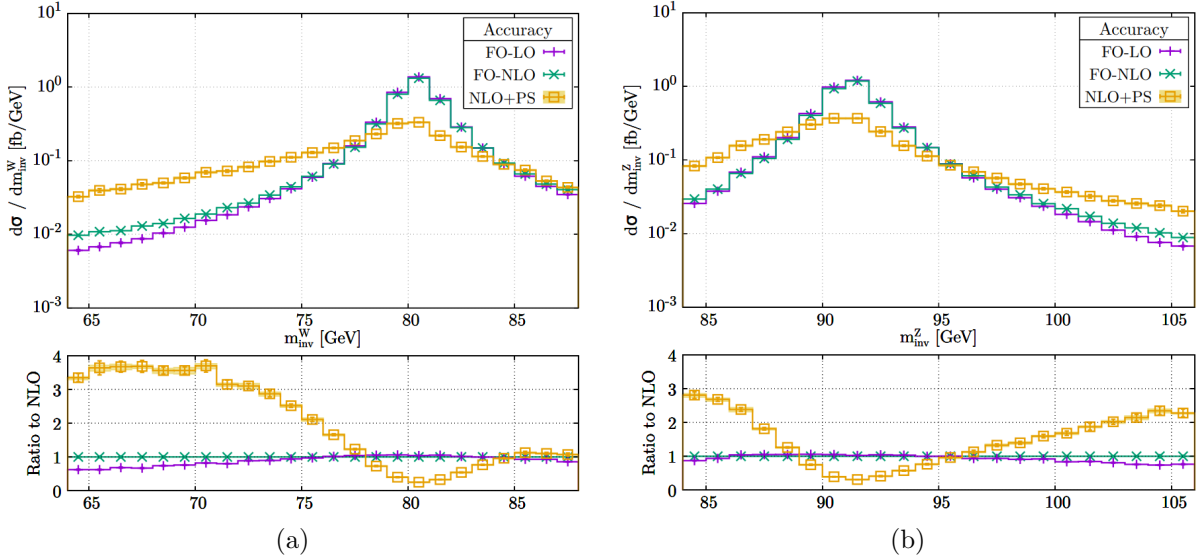


Figure 10: Predictions for VBS-induced  $W^+Z$  production in the fully hadronic decay mode at the LHC with  $\sqrt{s} = 13$  TeV within the cuts of eqs. (45)–(48) at LO (purple), NLO (green) and NLO+PS (orange). The upper panels show the reconstructed mass of the  $W$  boson (a), the reconstructed mass of the  $Z$  boson (b). The respective lower panels show the ratios of the LO and NLO+PS predictions to the NLO results.

semi-leptonic case, because now window cuts for both the  $Z$  and the  $W$  system have to be passed for an event to be accepted.

## 4 Conclusions and outlook

In this article we have presented new features for the implementation of VBS-induced  $WZjj$  production in the framework of the POWHEG BOX V2. We are providing semi-leptonic and fully hadronic decays of the intermediate vector bosons that were missing in the previously existing implementation, and account for physics beyond the SM by the inclusion of dimension-six operators of a generic EFT expansion in the EW sector.

To illustrate the capabilities of the updated implementation we considered some selected applications. We explored the sensitivity of typical VBS observables to dimension-six operators in an EFT framework, and found that, when the expansion is performed consistently, predictions with contributions from EFT operators compatible with current experimental limits barely deviate from the SM case at LHC energies. Larger effects are found at higher energies which could be achieved, for instance, at a future FCC.

Using the leptonic decay mode as an example, we investigated the relevance of including off-shell contributions and spin correlations in the simulation. By comparing our results to those obtained with the `MadGraph5_aMC@NLO+MadSpin` tool that combines a calculation of VBS-induced  $WZ$  production with a simulation of the gauge-boson decays we could show that the on-shell approximation is appropriate when all final-state leptons stem from the resonant decay of a gauge boson, but deviates from the full result in regions

away from the resonance. This limitation of the approximation should be kept in mind for ensuring its application is restricted to its region of validity.

Finally, we considered semi-leptonic and fully hadronic decay modes. We found that in these cases QCD corrections and PS effects can lead to a reshuffling of momenta such that they pass different selection cuts than the corresponding LO configurations. This kinematic effect results in a reduction of cross section beyond the LO, which becomes particularly pronounced once the NLO result is matched with a PS.

The new features of the VBS  $WZjj$  code will be made available via the POWHEG BOX V2 repository, see <https://powhegbox.mib.infn.it/>.

## Acknowledgements

We are grateful for valuable discussions with Johannes Scheller. We appreciate helpful input from our experimental colleagues, in particular Joany Manjarres. This work has been supported by the German Federal Ministry for Education and Research (BMBF) under contract no. 05H21VTCAA. The authors acknowledge support by the state of Baden-Württemberg through bwHPC and the German Research Foundation (DFG) through grant no INST 39/963-1 FUGG.

## References

- [1] ATLAS collaboration, M. Aaboud et al., *Observation of electroweak  $W^\pm Z$  boson pair production in association with two jets in  $pp$  collisions at  $\sqrt{s} = 13$  TeV with the ATLAS detector*, *Phys. Lett. B* **793** (2019) 469 [1812.09740].
- [2] CMS collaboration, A. M. Sirunyan et al., *Measurements of production cross sections of  $WZ$  and same-sign  $WW$  boson pairs in association with two jets in proton-proton collisions at  $\sqrt{s} = 13$  TeV*, *Phys. Lett. B* **809** (2020) 135710 [2005.01173].
- [3] ATLAS collaboration, G. Aad et al., *Search for the electroweak diboson production in association with a high-mass dijet system in semileptonic final states in  $pp$  collisions at  $\sqrt{s} = 13$  TeV with the ATLAS detector*, *Phys. Rev. D* **100** (2019) 032007 [1905.07714].
- [4] CMS collaboration, A. M. Sirunyan et al., *Search for anomalous electroweak production of vector boson pairs in association with two jets in proton-proton collisions at 13 TeV*, *Phys. Lett. B* **798** (2019) 134985 [1905.07445].
- [5] B. Jager, A. Karlberg and J. Scheller, *Parton-shower effects in electroweak  $WZjj$  production at the next-to-leading order of QCD*, *Eur. Phys. J. C* **79** (2019) 226 [1812.05118].
- [6] G. Bozzi, B. Jager, C. Oleari and D. Zeppenfeld, *Next-to-leading order QCD corrections to  $W^+ Z$  and  $W^- Z$  production via vector-boson fusion*, *Phys. Rev. D* **75** (2007) 073004 [hep-ph/0701105].

- [7] S. Alioli, P. Nason, C. Oleari and E. Re, *A general framework for implementing NLO calculations in shower Monte Carlo programs: the POWHEG BOX*, *JHEP* **06** (2010) 043 [1002.2581].
- [8] P. Nason, *A New method for combining NLO QCD with shower Monte Carlo algorithms*, *JHEP* **11** (2004) 040 [hep-ph/0409146].
- [9] S. Frixione, P. Nason and C. Oleari, *Matching NLO QCD computations with Parton Shower simulations: the POWHEG method*, *JHEP* **11** (2007) 070 [0709.2092].
- [10] C. Degrande, N. Greiner, W. Kilian, O. Mattelaer, H. Mebane, T. Stelzer et al., *Effective Field Theory: A Modern Approach to Anomalous Couplings*, *Annals Phys.* **335** (2013) 21 [1205.4231].
- [11] B. Jäger, A. Karlberg and G. Zanderighi, *Electroweak ZZjj production in the Standard Model and beyond in the POWHEG-BOX V2*, *JHEP* **03** (2014) 141 [1312.3252].
- [12] A. Denner, S. Dittmaier, P. Maierhöfer, M. Pellen and C. Schwan, *QCD and electroweak corrections to WZ scattering at the LHC*, *JHEP* **06** (2019) 067 [1904.00882].
- [13] K. Arnold et al., *VBFNLO: A Parton level Monte Carlo for processes with electroweak bosons*, *Comput. Phys. Commun.* **180** (2009) 1661 [0811.4559].
- [14] J. R. Andersen et al., *Les Houches 2017: Physics at TeV Colliders Standard Model Working Group Report*, [1803.07977].
- [15] A. Ballestrero et al., *Precise predictions for same-sign W-boson scattering at the LHC*, *Eur. Phys. J. C* **78** (2018) 671 [1803.07943].
- [16] J. Alwall, R. Frederix, S. Frixione, V. Hirschi, F. Maltoni, O. Mattelaer et al., *The automated computation of tree-level and next-to-leading order differential cross sections, and their matching to parton shower simulations*, *JHEP* **07** (2014) 079 [1405.0301].
- [17] R. Frederix, S. Frixione, V. Hirschi, D. Pagani, H. S. Shao and M. Zaro, *The automation of next-to-leading order electroweak calculations*, *JHEP* **07** (2018) 185 [1804.10017].
- [18] P. Artoisenet, R. Frederix, O. Mattelaer and R. Rietkerk, *Automatic spin-entangled decays of heavy resonances in Monte Carlo simulations*, *JHEP* **03** (2013) 015 [1212.3460].
- [19] P. Skands, S. Carrazza and J. Rojo, *Tuning PYTHIA 8.1: the Monash 2013 Tune*, *Eur. Phys. J. C* **74** (2014) 3024 [1404.5630].
- [20] M. Cacciari, G. P. Salam and G. Soyez, *FastJet User Manual*, *Eur. Phys. J.* **C72** (2012) 1896 [1111.6097].

- [21] M. Cacciari, G. P. Salam and G. Soyez, *The anti- $k_t$  jet clustering algorithm*, *JHEP* **04** (2008) 063 [0802.1189].
- [22] NNPDF collaboration, R. D. Ball et al., *Parton distributions from high-precision collider data*, *Eur. Phys. J. C* **77** (2017) 663 [1706.00428].
- [23] A. Buckley, J. Ferrando, S. Lloyd, K. Nordström, B. Page, M. Rüfenacht et al., *LHAPDF6: parton density access in the LHC precision era*, *Eur. Phys. J. C* **75** (2015) 132 [1412.7420].
- [24] CMS collaboration, A. Tumasyan et al., *Measurement of the inclusive and differential WZ production cross sections, polarization angles, and triple gauge couplings in pp collisions at  $\sqrt{s} = 13$  TeV*, *JHEP* **07** (2022) 032 [2110.11231].
- [25] A. Sirunyan, A. Tumasyan, W. Adam, F. Ambrogio, T. Bergauer, M. Dragicevic et al., *Measurements of production cross sections of WZ and same-sign WW boson pairs in association with two jets in proton-proton collisions at  $\sqrt{s} = 13$  tev*, *Physics Letters B* **809** (2020) 135710.
- [26] B. Feigl, *Anomale Vier-Vektorboson-Kopplungen bei der Produktion von drei Vektorbosonen am LHC*, Diplomarbeit, KIT, 2010.
- [27] O. Schlimpert, *Anomale Kopplungen bei der Streuung schwacher Eichbosonen*, Diplomarbeit, KIT, 2013.
- [28] J. Baglio et al., *VBFNLO: A Parton Level Monte Carlo for Processes with Electroweak Bosons – Manual for Version 2.7.0*, 1107.4038.
- [29] J. Baglio et al., *Release Note - VBFNLO 2.7.0*, 1404.3940.
- [30] ATLAS collaboration, G. Aad et al., *Measurements of  $W^\pm Z$  production cross sections in pp collisions at  $\sqrt{s} = 8$  TeV with the ATLAS detector and limits on anomalous gauge boson self-couplings*, *Phys. Rev. D* **93** (2016) 092004 [1603.02151].
- [31] B. Jäger, L. Salfelder, M. Worek and D. Zeppenfeld, *Physics opportunities for vector-boson scattering at a future 100 TeV hadron collider*, *Phys. Rev. D* **96** (2017) 073008 [1704.04911].